Dust Flux Monitor Instrument measurements during Stardust-NExT Flyby of Comet 9P/Tempel 1

Journal Item

Dust Flux Monitor Instrument measurements during Stardust-NExT Flyby of Comet 9P/Tempel 1

Thanasis E. Economou[1], Simon F. Green[2], Don E. Brownlee[3], Ben C. Clark[4]

[1]Laboratory for Astrophysics and Space Research, Enrico Fermi Institute, University of Chicago, 933 East 56th St, Chicago IL 60637, USA.

[2]Planetary and Space Sciences, Department of Physical Sciences, The Open University, Walton Hall, Milton Keynes, MK7 6AA, UK.

[3]Deparment of Astronomy, University of Washington, Seattle WA 98195,USA.

[4]Space Science Institute, Boulder CO 80301, USA.

Accepted for publication in Icarus

2012

Abstract

The Dust Flux Monitor Instrument (DFMI) on the Stardust and Stardust-NExT missions measured impacts from coma dust particles with masses from ~10^{-15} to >10^{-6} kg using two kinds of sensors – one based on polyvinylidene fluoride (PVDF) thin films and the other on acoustic detectors (ACs) mounted on the front and second layers of the Whipple Bumper Shield. At the higher encounter speed of 10.9 km s^{-1} at Comet 9P/Tempel 1 compared with 6.12 km s^{-1} at 81P/Wild 2 encounter, the mass sensitivity of DFMI sensors increased by between a factor of 2 and 12 (depending on the sensor subsystem), but the spatial resolution (≥1.09 km) decreased to approximately a half. The coma of Comet Tempel 1 exhibits highly non-uniform spatial distribution of dust, as found at comet Wild 2, with bursts of impacts of up to 1000 particles over km scales near closest approach surrounded by void regions of many kilometers with no impacts. These data are consistent with passage through clouds of particles resulting from fragmentation of larger aggregates emitted from the nucleus. These fragmentation products dominate the total dust production of small particles, with only a small contribution likely from direct emission from the nucleus. The derived overall mass distribution is similar to that found at comet Wild 2 with the total mass dominated by large particles. The average cumulative mass index $\alpha = 0.65 \pm 0.08$ (where the particle flux is defined by $\phi\,(>m) = k\,m^{-\alpha}$) but a better fit is obtained with $\alpha = 0.85 \pm 0.08$ for particle masses below 10^{-10} kg and a significantly lower value for higher masses.

1. Introduction

The Dust Flux Monitor Instrument on the Stardust-NExT mission is the same instrument that provided information on the coma dust particle flux, intensity profile and mass distribution during the encounter with comet Wild 2 in January 2004. While the total dust fluence during that

flyby was comparable with pre-encounter predictions based on the observed coma brightness, DFMI did not detect the expected relatively smooth rise and fall in impact fluxes. The fluxes exhibited very large fluctuations with rates of hundreds of counts per second for short periods separated by intervals with no detected impacts (Tuzzolino *et al*., 2004). The impact rates were characterized by "swarms" lasting up to a few seconds consisting of a number of separate "bursts" of impacts lasting of order 0.1 s. These were interpreted as the result of passage of the spacecraft through a combination of jets (Sekanina et al., 2004) and expanding clouds of debris from grain fragmentation (Clark *et al*., 2004; Green *et al*., 2004).

After the end of the Stardust mission on January 15, 2004, with the successful recovery of samples from the Earth Re-entry Capsule (Brownlee *et al*., 2006), DFMI, as well as the other Stardust payload instruments, were functioning nominally. The spacecraft which was also in excellent condition and with enough fuel reserves that could be used to control it for a long time was redirected towards an encounter with Comet Tempel 1, previously visited by the Deep Impact spacecraft in 2005. Comet Tempel 1 therefore became the first comet in history to be visited and investigated twice by two sets of instruments on two different missions.

The DFMI during the Tempel 1 flyby was turned on at 04:17:16.4 UT on 15 February 2011, 22 min before the closest approach at 04:39:12 and operated for 40 min before it was turned off at a distance of about 11,700 km from the comet. During that period it provided flux information with all its counters with a time resolution of between 1 and 0.1 s, from which the cometary dust particle mass distributions were derived. We describe the instrument and sensor subsystem detection methods in Section 2 followed by the modifications to the instrument calibration required for the Tempel 1 encounter in Section 3. The initial results of the spatial and mass

distributions of detected coma dust are presented in Section 4 and compared with the results from Wild 2.

2. Instrument description

The Dust Flux Monitor Instrument (DFMI) on Stardust-NExT measured impacts from cometary dust particles as the spacecraft passed through the coma of Comet P/Tempel 1. The spacecraft orientation and high speed relative to the cometary dust particles meant that, as at P/Wild 2, all impacts were from a direction within a few degrees of perpendicular to the front shield and detectors.

DFMI uses two kinds of sensors – one based on polyvinylidene fluoride (PVDF) thin films and the other on acoustic detectors (ACs). PVDF sensor subsystem comprises two circular thin films, one 6 μm thick and of area 20 cm^2 and the other 28 μm thick and of area 200 cm^2, with four different mass thresholds each (m1-m4 and M1-M4). The two acoustic sensors are mounted on the front and second protective shields (with sensitive area approximately 0.3 m^2 and 0.7 m^2 respectively) with two mass thresholds each (AC_1-AC_4). Particles reaching the second shield have to penetrate the front shield. Fig. 1 shows the location of the payload instruments on the Stardust spacecraft. The DFMI instrument was described in more detail by Tuzzolino et al., (2003).

2.1 PVDF sensor system

The PVDF sensor system is based on polyvinylidene fluoride thin film material with built-in polarization that is capable of detecting high-velocity dust particles. The dust particle detection technique was developed at the University of Chicago by Anthony Tuzzolino and is described in

detail by Simpson and Tuzzolino (1985). The PVDF sensor system for the Stardust mission consists of two circular frames that are rigidly mounted to the spacecraft Bumper Shield where they are exposed to the dust particle flux during the encounter with a comet. The PVDF films themselves, however, are supported by foam padding to isolate them acoustically from outside noise. The signals from the PVDF sensors are fed by a long cable to the DFMI electronic stored inside a thermally-controlled box. The cable length required a special kind of first stage amplification circuitry to handle the large input capacitance.

The amplified signals for each sensor system are fed to their appropriate counters through threshold setting discriminators. For each sensor unit there are four mass threshold levels (m1-m4, M1-M4) that help to determine the mass distribution of the comet dust particles. The amplitude of the signal from the PVDF counters is a function of mass and the velocity of the dust particles. Because the ejection velocity from the comet is small, it is assumed that the particles impact DFMI at the spacecraft encounter velocity with the comet. The precise knowledge of the velocity enables determination of the mass of the dust particle from the signal amplitude for each counter. At the encounter speed of 10.9 km s^{-1}, the DFMI mass measurements extend over 9 decades, from ~10^{-15} to >10^{-6} kg.

The PVDF sensors have a maximum time resolution of 0.1 seconds and the ability to handle up to 10^4 counts per second without any appreciable dead time. When an impact is detected, the counter for the appropriate mass channel is incremented by 1. All counters are read out either at 1 s (cruise mode) or at 0.1 s (encounter mode) time intervals.

The DFMI has a built in In-Flight Calibrator (IFC) for occasional checking of the proper operation and stability of its electronic circuitry. The IFC was used periodically throughout the entire flight period on both missions.

2.2 Acoustic sensor system The dual acoustic sensor system (DASS) consists of two quartz piezoelectric acoustic sensors mounted on the rear of one half of the front bumper shield within the launch adapter ring (A1) and on a circular sounding sheet attached in front of the first NEXTEL curtain immediately behind the front bumper shield (A2). The A2 sensor is behind the A1 sensor and a signal on A2 only occurs when a particle has penetrated the front bumper shield.

An understanding of the operation of the acoustic sensors is required to interpret the results. The counts produced by the on-board software are not a direct record of the number of impacts detected. An impact on the active half of the front shield produces a vibration which is detected by sensor A1. The output voltage obtained from the sensor is a complex sinusoidal oscillation at frequency ~20 kHz within a decaying envelope, which has an initial sharp rise to a peak voltage V_p, and a gradual quasi-exponential decay with a time constant of a few milliseconds. V_p is related to the particle impact momentum and position on the shield. The limitations on mass and data rate for the acoustic subsystem mean that V_p cannot be measured over a large dynamic range. Instead, the waveform is characterized by two counts, "AC_1" and "AC_2". If the output voltage exceeds the threshold V_1 during a fixed time interval T_1, then AC_1 is incremented by 1, and similarly for time interval T_2 and AC_2 (see Fig. 2). Thus AC_1 (or AC_2) represents the number of time intervals over which the signal is (at some time during the interval) above the voltage threshold V_1 (or V_2). A large impact will produce a large V_p and a long duration signal giving a large change in AC_1 and AC_2, whereas a small signal will produce only a small change in AC_1. The encounter data consist of AC_1 and AC_2 cumulative counts at the end of sample read-out

periods of between 0.1 and 1.0 s depending on the signals detected by the PVDF sensors. T_1 and T_2 are 510 and 210 μs respectively, giving maximum possible AC_1 and AC_2 values of 1960 and 4762 in 1 s read outs. However, the AC_1 and AC_2 counters were restricted to 8 bits (256 increments) so it was possible that multiple or very large events could cause the counters to overflow.

The rear shield produces counts, AC_3 and AC_4, in a similar way to those on the front shield. However, the sensor will only be triggered if an impacting particle penetrates the front shield and the resultant ejecta (and possible particle remnants) produce a signal sufficiently large to trigger the detector.

The numbers of impacts, N_1 to N_4, that produce these recorded counts are determined from inspection of the transmitted counts. The analysis uses a variety of information (the AC_1/AC_2 and AC_3/AC_4 ratios; consistency of signals for penetrating impacts; number of counts in time interval (T_1, T_2) vs. maximum number possible to assess whether more than one impact occurred during the sampling period and if so the likely number of impacts in this step and the possibility of overflow of counts from an impact in one time step to the next time step. Examples of this analysis are included in Section 4.2.

The calibration of the acoustic sensors (derivation of mass thresholds and effective areas) from which the particle flux and mass distribution can be derived, is described in Section 3 below.

3. Calibration

3.1 PVDF sensor system

The derivation of flux (number of impacts per m^2 per second), or fluence (time integrated flux), for the PVDF sensors is relatively straightforward. The sensors were calibrated using the dust accelerators at Heidelberg and Munich (see Simpson et al., 1985). Two sets of calibration data were obtained for the 20 cm^2, 6 μm thick small PVDF sensor "m" and for the 200 cm^2, 28 μm thick larger PVDF sensor, designated "M" using carbonyl iron or iron dust particles accelerated at Heidelberg and glass particles at Munich (see Tuzzolino et al. (2003). From the calibration data analytical expressions were obtained for the number of electrons released, N_e, that best fit the experimentally obtained calibration data:

$$N_e = \mathrm{k}\, m^a\, v^b \qquad (1)$$

where *a = 1.3 and b =3.0 for Fe particles on the 6* μm sensor (for 10^{-16} kg < *m* < 10^{-12} kg)

a = 0.7 and b =3.0 for glass particles on the 6 μm sensor (for 10^{-12} kg < *m* < 10^{-8} kg)

a = 1.3 and b =3.0 for Fe particles on the 28 μm sensor (for 10^{-16} kg < *m* < 10^{-12} kg)

a = 0.9 and b =3.0 for glass particles on the 28 μm sensor (for 10^{-12} kg < *m* < 10^{-9} kg)

and k is a constant.

Since the velocity, *v*, is assumed to be given by the encounter velocity of the spacecraft relative to the comet, the mass of an impacting dust particle can be uniquely determined from the measured signal amplitude. The mass thresholds for the PVDF counter channels were determined for the original Stardust mission to get the optimal size distribution of dust particles from comet Wild 2 with an encounter velocity of 6.1 km s^{-1}. These thresholds are shown in Table 1.

The only uncertainty in this type of calibration is the use of solid particles of higher density during the accelerator calibration vs the actual density of the cometary particles that will be both lower and variable. Although the mass thresholds were well defined (±10%) from the calibration,

177 they were derived from impacts of high-density particles. The signal is proportional to the
178 volume of depolarisation, which in turn is approximately proportional to particle size. The
179 density of comet dust particles measured by samples returned by Stardust from comet Wild 2
180 ranged from metallic iron with a density of ~8000 kg m^{-3} to aggregates that may have densities
181 less than 1000 kg m^{-3}. Typical silicate particles should have densities in the 3500 - 1000 kg m^{-3}
182 range. Due to the unknown density we have assigned uncertainties of a factor of two in mass to
183 each threshold.

184 **3.2 Acoustic sensor system**

185 The derivation of the mass of an individual impacting particle on the acoustic sensors
186 requires knowledge of the impact position and the detector sensitivity. Since the position is
187 unknown, a given signal, characterized by *V*p or AC_1 (and possibly AC_2), may be the result of a
188 small impact close to the sensor or a large impact further away. The derived momentum (and
189 hence mass) of an impactor is therefore represented by a probability function rather than a
190 specific value. This is also true for the mass thresholds corresponding to events that just trigger
191 the sensor (i.e. AC_1=1). For a given particle mass, the sensitive area of the shield was obtained
192 from absolute momentum calibration, obtained with the University of Kent Light Gas Gun
193 (LGG) shots at a fixed distance from a sensor on a small section of flight-representative shield,
194 combined with relative signal attenuation as a function of impact position, obtained from 'bead
195 drops' over the whole shield. Preliminary calibration is described by McDonnell *et al.* (2000)
196 and Tuzzolino *et al.* (2003) and the calibration used for the comet Wild 2 encounter data is
197 described by Green *et al*. (2004).

198 The mass threshold (m_i) of a small area element (i) on the shield is given by

199 $$m_i = V_T / (\varepsilon\, S\, v\, R_i) \qquad \text{for } m_i < m_{pen} \qquad (2)$$

$$m_i = [\ V_T /(\ \varepsilon\ S\ v\ R_i\ (m_{pen})^{\gamma})\ ]^{(1/(1-\gamma))} \qquad \text{for } m_i > m_{pen} \tag{3}$$

where V_T is the output voltage for the threshold detection, S is the absolute sensitivity of the detector (in fact εS is measured) at a defined distance from the sensor, R_i is the relative sensitivity of the shield element, ε is the momentum enhancement factor, v is the impact speed, m_{pen} is the mass at which the shield is just penetrated and γ is the momentum derating factor.

For particles that penetrate the shield, the momentum enhancement factor (due to the additional momentum of ejecta released during the impact must be derated to account for the momentum that is transferred through the target and not captured:

$$\varepsilon' = \varepsilon\,(m_{pen}/m)^{\gamma} \tag{4}$$

A value of $\gamma = 0.4 \pm 0.1$, derived from Giotto data (*Perry*, 1990), was adopted for the Wild 2 encounter. The particle momentum (and hence mass) was known for the LGG impact calibration tests which were conducted at ~6 km s^{-1}. However, the measured signal implicitly included momentum enhancement at the same level as was experienced in the Wild 2 flyby and hence eliminated uncertainty in the value of ε at that encounter.

Detection thresholds are set in the flight electronics, which are equivalent to a high sensitivity channel voltage threshold $V_1 = 0.005$ V and a low sensitivity channel voltage threshold $V_2 = 0.05$ V for the unamplified sensor output. As the speed of the impactor is known, then m_i can be determined.

The effective area of the acoustic sensor subsystem is required in order to derive a particle flux or fluence (number of particles per unit area) from the observed number of impacts. The *sensitive* area of an acoustic detector is equal to the entire area of the acoustically linked portion of the shield for very large particles. However, for impactors of lower mass, the impact signal will only be above the threshold voltage for detection if the impact occurs close to the

sensor. The sensitive area of the detector is therefore dependent on particle mass (for a fixed impact speed as is the case with a comet encounter). The relationship between the observed number of particles (i.e. those producing signals above the detection threshold) and the true number impacting the shield will therefore depend on the mass distribution.

The effective area for a given sensor channel, which is a function of mass, is defined as the area required to convert the number of impacts detected by that channel to the true impacting flux or fluence. In order to determine the effective area we assume a cumulative mass distribution function for the impacting particles of the form:

$$\phi\,(>m) = k\,m^{-\alpha} \qquad (5)$$

where $\phi\,(>m)$ is the flux (number per m^2 per second) of particles larger than or equal to mass m, and k is a constant. For each surface element of the shield, the mass required to produce the threshold signal is calculated using Eqs. 2 or eq. 3, and hence the total number of particles detected from that surface element can be calculated. Combining the results from all the surface elements produces the total number of detections as a function of mass. The limiting mass corresponds to the mass threshold for the most sensitive surface element but has a very small sensitive area, so only a small fraction of the impacts that occur at this mass are detected. We define an effective mass limit, m_{eff}, where approximately 50% of particles impacting the shield are detected (between 30% for α=1 and 70% for α=0.25). 96% of all particles impacting the shield are larger than this mass for α=1, and over 99% for α<0.5. The effective area, $A_{\mathrm{eff}}(\alpha)$, can then be calculated at a mass of m_{eff} for an assumed value of the mass distribution index α.

As the *actual* mass distribution is unknown, the calculation of effective area is iterative. An initial value of α is assumed, and the fluences calculated, which defines the empirical mass distribution index, which can be fed back into a new calculation of effective area. Green et al.

(2004) chose the threshold masses in a similar way for the Wild 2 encounter. There is some uncertainty in the threshold mass for acoustic channel 1 because the LGG calibration shots to determine the absolute sensitivity *S*, used aluminum spheres, whereas the cometary particles are likely to have rather different physical properties. A conservative value of a factor of 3 was therefore applied to m_{eff} for both channels of the front shield sensor, i.e. $m(AC_1)$ and $m(AC_2)$. However, the ratio $m(AC_2)/m(AC_1) = 10$ is precisely defined by the choice of threshold voltages V_1 and V_2.

The mass threshold for the rear shield sensor $m(AC_3)$ was determined for the Wild 2 encounter using LGG impacts with a range of materials to determine the ballistic limit (penetration threshold) of the bumper shield material The exit hole area was measured as a function of particle momentum and the mass threshold was chosen to correspond to the point where the impactor mass (for an impact speed of 6.12 km s^{-1}) caused a hole of non-zero area (see Tuzzolino et al., 2003 for preliminary analysis). The uncertainty is based on the scatter in the limited experimental data for different impactor materials. The mass threshold for AC_4 is fixed at precisely 10 times that of AC_3. The effective area of the rear shield sensor is not known since it was not possible to conduct hypervelocity impact tests due to the large size of the shield (and the need to retain its integrity for future calibration!). However, constraints were placed on the effective area from the maximum size of the shield (0.7 m^2) and the size of expected ejecta cones, which gives a minimum area ~0.1 m^2. An effective area of ($0.3\ ^{-0.2}/_{+0.4}$) m^2 was therefore adopted for the Wild 2 encounter data.

3.3 Mass thresholds and effective areas for 9P/Tempel 1 encounter

The operations of the DFMI at Tempel 1 were essentially identical to those at the successful Wild 2 encounter. However, the sensitivity of each subsystem is affected by the difference in encounter speeds (10.9 km s^{-1} at Tempel 1 vs. 6.12 km s^{-1} at Wild 2). The sensitivity increases because of the velocity dependence of the measured signals.

For the PVDF sensors, the detected signal is the number of electrons is given by equation (1), so the mass thresholds for the Tempel 1 encounter, m(T1) are related to those at Wild 2, m(W2), by

$$m(\mathrm{T1}) = m(\mathrm{W2})\ (v(\mathrm{W2})/v(\mathrm{T1}))^{b/a}. \qquad (6)$$

which gives $m(\mathrm{T1}) = 0.264\ m(\mathrm{W2})$ for the 6 μm PVDF sensor channels m1 and m2,

$m(\mathrm{T1}) = 0.084\ m(\mathrm{W2})$ for the 6 μm PVDF sensor channels m3 and m4,

$m(\mathrm{T1}) = 0.146\ m(\mathrm{W2})$ for the 28 μm PVDF sensor channels M1 to M4,

using the values of a and b for the appropriate mass ranges. The sensitive areas of the PVDF sensors are defined by the geometry of the detectors and remain unchanged.

A new calibration campaign for the acoustic sensors was not possible for the Tempel 1 encounter because the limiting speed of an LGG is well below the encounter speed. For a given (non-penetrating) impact, the mass threshold at Tempel 1 can be obtained by scaling. Using Eq. 2, the mass threshold for Tempel 1 is given by:

$$m_i(\mathrm{T1}) = m_i(\mathrm{W2})\ [\varepsilon(v(\mathrm{W2}))/\varepsilon(v(\mathrm{T1}))]\ [v(\mathrm{W2})/v(\mathrm{T1})]. \qquad (7)$$

The momentum enhancement factors applicable for each encounter are not known. For the Wild 2 encounter the LGG calibration shots implicitly contained the enhancement factor. For the derivation of the mass thresholds at Tempel 1, we need an estimate of $\varepsilon(v(\mathrm{W2}))/\varepsilon(v(\mathrm{T1}))$. Walker

292 and Chocron (2011) present experimental results for momentum enhancement for a number of
293 impact speeds up to 8 km s^{-1} together with CTH computations up to 10 km s^{-1} and a range of
294 target and impactor materials including metals, rocks and polymers. Although the complex
295 structure of the Stardust shield is not represented by the targets, the range of results for different
296 target and impactor densities and compressive strengths gives an indication of the potential range
297 in the ratio of enhancements at the two impact speeds. Interpolating the results to speeds of 6.1
298 and 10.9 km s^{-1} we derive the ratio $\varepsilon(v(\mathrm{W2}))/\varepsilon(v(\mathrm{T1}))$ for 18 different combinations of target and
299 impactor which lie in the range 0.96 to 0.64. This factor and range are sufficiently small that
300 they are not major contributors to the uncertainty in the mass calibration and we adopt
301 $\varepsilon(v(\mathrm{T1}))/\varepsilon(v(\mathrm{W2})) = 0.8 \pm 0.15$ in this analysis. The DFMI mass thresholds for the A1 sensors are
302 therefore given by $m_{\mathrm{i}}(\mathrm{T1}) = 0.45\, m_{\mathrm{i}}(\mathrm{W2})$.

303 The mass threshold for penetration of the front shield is determined by the ballistic limit
304 of the front shield. A number of different empirical relationships have been derived that fit
305 laboratory data. These equations are a function of impactor mass size and impact velocity as well
306 as physical properties of the target and impactor (see e.g. McDonnell *et al.* 2001). Although the
307 equations take a variety of forms they can, for normal incidence impacts and fixed target and
308 impactor properties, generally be reduced to the form $m_{\mathrm{pen}} \propto v^{b}$. An analysis of eight different
309 functions gives a mean value of the exponent b of –2.0 with standard deviation of 0.3. We
310 therefore conclude that penetration is, to first order, linked to the impact energy of the impactor.
311 Fig. 3 illustrates the exit hole area as a function of impact energy for normal impacts of different
312 projectiles onto the Stardust shield material using the LGG. The impact speeds were in the range
313 4.0 to 6.2 km s^{-1}. The estimated kinetic energy for a marginally penetrating particle is $(7\ ^{+7}/_{-4})$ J.
314 In the absence of any feasible tests for the rear shield sensor sensitivity, we make the assumption

that a marginal penetration produces sufficient forward ejecta to trigger a signal. This yields m_{pen} = ($2^{+2}/_{-1.2}$) x 10^{-7} kg for the Wild 2 encounter and m_{pen} = ($6^{+6}/_{-4}$) x 10^{-8} kg for the Tempel 1 encounter.

Table 1 shows a comparison of the mass thresholds for the two encounters and the effective sensor areas. It also shows the dust particle fluence for the Tempel 1 encounter for each mass threshold. Fig. 4 shows the effective area for the acoustic sensor channels AC_1 and AC_2 as a function of mass distribution index α.

4. Tempel 1 encounter results

4.1 Instrument performance

The Dust Flux Monitor Instrument performed well during the encounter with Comet Tempel 1 and provided valuable dust particle flux information and dust particle size distribution of the comet material. The DFMI was one of the three payload instruments on Stardust-NExT mission besides the navigation camera and the Cometary and Interstellar Dust Analyser (CIDA). The DFMI was turned on at 4:17:01, just 22 minutes and 11 sec (~14,000 km along track) before the closest approach, but the first particle detection was at 4:32:35.4, 397 seconds (~4300 km) before closest approach at 4:39:12 by the acoustic counter AC1. It was turned off at 4:57:01, but most of the activity was concentrated on all mass thresholds within ±40 seconds (±436 km) from the time of closest approach.

The first PVDF event was detected on counter m1 at 4:37:54 at a distance of only about 850 km from the closest approach. The DFMI registered a total of 4393 events most of which were close to the lowest mass threshold (< 10^{-14} kg), although a few were massive enough (>10^{-7}

kg) to penetrate the front shield. The instrument performed nominally until 4:44:28 (+3438 km from the closest approach) when it started to exhibit the expected and familiar noise pattern identified during cruise phase.

About 4 months into the original Stardust mission, the DFMI suddenly developed a noise problem that affected its performance: after normal operation for about 35-40 min, the DFMI became very noisy and unstable (see Fig. 5a). An enormous effort by the project, the spacecraft engineers and University of Chicago technical personnel was undertaken to understand the nature of this noise problem. After some detective work, it was traced to a break in the cooling path of the power supply that overheated after 35-40 min of operation and caused thermal noise. However, since the instrument operated normally until the sudden onset of noise, the encounter operations were modified to place closest approach within the nominal operation period of about 35 min. Occasional IFC calibrations were performed indicating nominal performance of the DFMI throughout the entire periods of the Stardust and Stardust-NExT missions. Fig. 5b compares the IFC calibration data during the Annefrank asteroid encounter in January 2003, before the encounter with Comet Wild 2, with the calibration data in January 2007, at the beginning of the Stardust NExT mission. As it can be seen, there is no change in the performance of the DFMI during the intervening 4 years in space. Similarly, Table 2 compares the IFC calibration data, on 2 February 2011, just before the encounter with Comet Tempel 1, with those taken in 2002 and 2010. Again, the data confirm no change in the performance of the DFMI during the 9 years of operation in space and at the encounter with Comet Tempel 1 it was the same as it was at the beginning of the mission. The numbers associated with each PVDF counter in Table 2 are digital representation of artificially induced analogue signals in the front of the DFMI electronics and can tell only the correct performance of the electronics, but not the

sensors. The numbers on the table are the final levels reached during the IFC calibrations for each PVDF counter. The nominal performance of the DFMI was also confirmed by the S/C monitoring of the DFMI current usage (Allan Chevraunt, private communication), that showed increased currents only during the ±40 seconds when the DFMI was most active.

Only data obtained at the Tempel 1 encounter before the onset of the noise is included in the following analysis.

The PVDF 6 μm sensor recorded 4186 impacts over all four channels, with the majority in the most sensitive channel, m1. The 28 μm sensor recorded just 13 impacts with all but one in the channel M1. There were no counter overflows and the maximum count rates did not exceed 10^4 per second.

In order to determine the impact rates for the acoustic sensors, the time intervals where counts were detected must be considered individually. In total, 117 time intervals contained non-zero AC_1 counts, 63 contained non-zero AC_2 counts, 18 contained non-zero AC_3 counts and 4 contained non-zero AC_4 counts. In all cases where AC_3 was non-zero there was a signal in AC_1 and AC_2 in the same or a preceding time step, indicating that the penetrations detected by the rear shield A2 sensor were also detected by the A1 sensor. Although it was possible for multiple or large events to cause the 8 bit acoustic sensor counters to overflow more than once during one time interval (i.e. counts exceeding 255), there is no evidence for this occurring even during the highest activity periods. The largest individual counts were AC_1=136, AC_2=159, AC_3=80 and AC_4=69. (The AC_1 counters overflowed 15 times during the course of the encounter, the AC_2 counter six times and the AC_3 counter once). The data are best explained by $N_1 = 124+n$ impacts, where n is some small but undetermined number of impacts with very low signals, close to the

detection threshold and thus ‘hidden’ among the signals from the larger unambiguously detected particles.

Table 3 lists selected time periods during the encounter to illustrate how the number of impacting particles was constrained from the acoustic sensor signals AC_1-AC_4:

Record 920: Single isolated event in channel AC_1 with no PVDF counts in time interval.

Records 1239 and 1240: Signals detected in adjacent time steps. There is a possibility of this being a single event (i.e. occurring close to the end of record 1239 with the AC_1 signal overflowing into record 1240). However, the probability of two events is higher, based on the total duration of each interval so this is recorded as two events in with N_1=2 and N_2=1 (with a minimum possible number of events N_1=1, N_2=1).

Records 1269 and 1270: AC_1 and AC_2 counts in records 1269 and 1270. Could be two separate events or an overflow. The AC_2/AC_1 ratio is out of expected range (based on isolated impacts and laboratory tests) for record 1269, which indicates there is an overlap of channel 2 counts. In this case, both the start and end times for AC_1 and AC_2 signals must be coincident (duration 8.0 ms). This leaves 2.2 ms (= 4 counts) of AC_1 signal, which must be a separate event. If all the counts in record 1240 are from the same event, this gives AC_1=76, AC_2=56 and an AC_1/AC_2 ratio within expected range. We assign this as the minimum likely number of events to explain the data (i.e. N_1=2, N_2=1 in record 1269 and no event in record 1270. Another possibility is that only AC_1 overflows giving 1 event (N_1=1 and N_2=1) in record 1269 and a second event (N_1=1, N_2=1) in record 1270. The former case is higher probability (only one AC_2 event) so this is adopted.

Records 1282 to 1287: Record 1282 most likely contains a single impact. Possible overlap into record 1283 but very low probability. Record 1283 has signals in all 4 channels. However, AC_3

406 must be an overflow into record 1284 and this makes things more complicated. 80 counts in AC_3
407 last 40.8 ms. The AC_2 counts of 142 last 29.8 ms so this is consistent with zero overflow. AC_1
408 counts can be no greater than 80 from this overlapping event. This gives 39 counts in AC_1 for
409 another event in record 1283. The AC_1/AC_2 ratio is slightly lower than expected but any other
410 solution is worse. All the signals in record 1284 are assigned to the event in record 1283 (an
411 AC_3 count without AC_2 means it must be an overflow from the previous record). Record 1285
412 might be interpreted as a single marginal shield penetration. However, the AC_1/AC_2 ratio is low,
413 which indicates a possible overlap with the next record. Record 1286 has AC_1 counts that are
414 high for an event with AC_2=0. We assign half these counts to the impact in record 1285 with
415 remainder assigned to this record. For record 1287, a separate single impact is most probable.
416 The minimum number of impacts that could have produced all the received acoustic sensor
417 signals is N_1=106 although this requires a number of low probability events. Consideration of the
418 individual AC counts gives a best solution with N_1 = 125 and an estimated upper limit to N_1 of
419 161. The derived number of particles triggering the AC_2 channel, N_2 = 61. A derived total of 17
420 particles penetrated the front shield and were detected by the A2 sensor channel AC_3 (N_3), 4 of
421 which were also detected in channel AC_4 (N_4). For the determination of the encounter fluence we
422 therefore adopt $N_1 = 125\ ^{+36}/_{-18}$, $N_2 = 61\pm8$, N_3=17±4 and N_4 = 4±2. The assigned uncertainties
423 are based on $\sqrt{N}$ statistical uncertainties for channels 2 to 4 and the expected range of events for
424 channel 1.
425 As at P/Wild 2, the total fluence detected at Tempel 1was consistent with estimates based
426 on ground-based observations of the dust coma.
427 Although CIDA was not designed to determine fluxes, the total number of spectra detected
428 at comet Wild 2 were not consistent with the approximate mass threshold expected for the

instrument (Green et al. 2007). The reason for the very low flux compared with DFMI and the cratering data remains unexplained. The flux implied by the number of spectra detected at Tempel 1 was similarly low compared with DFMI. At comet Wild 2, it was possible to compare the independent determinations of particle size inferred from the impact sites on foils and aerogel in the returned samples. The fluxes are in excellent agreement for sizes above about 20 μm, whereas DFMI over-predicts the cratering rate at the smaller sizes by up to an order of magnitude (Horz et al. 2006). Over-simplification of calibrations (e.g. for crater/entry site to particle size, see Price et al. 2010; DFMI subsystems; particle densities) resulting from the difference in behavior between real particles and those used in the calibrations may explain at least some of this discrepancy.

4.2 Spatial distribution

Fig. 6 is a 3D figure showing all the DFMI data obtained during the encounter. The x-axis indicates the time in seconds from the closest approach. As expected, most of the dust activity is concentrated within ±40 s from the closest approach with very little activity outside that region. The y-axis indicates the mass of the dust particles sorted according to their weight: the lightest and most prominent particles (from m1 counter are plotted in back, while the heaviest (from AC4 counter) are plotted in front. The z-axis indicates the dust intensity, in counts/s. The raw data from which the rates were derived were submitted to PDS and can be found at Economou et al. (2011). The data show a similar pattern to what was seen during the encounter with comet Wild 2 in 2004 (Tuzzolino, et al., 2004) with bursts of large numbers of impacts separated by quiescent periods, rather than a smooth rise and fall in activity.

Fig. 7 illustrates the counts received by all the sensors during a short period around closest approach. There are two characteristics of the count rates that are immediately apparent: the asymmetry about closest approach and the nature of the bursts of events. The peak impact rates occur a few seconds after closest approach, but fall off rapidly. The asymmetry is most marked for the smaller (micro-sized) particles detected with the PVDF sensors. The encounter geometry, with a solar phase angle on approach of 81.6° is almost symmetrical with respect to the subsolar point (passed at 2.4 s before closest approach). The asymmetry is not therefore a result of local terminator crossing, but reflects non-uniform emission from the comet's surface. The impacts occur in clusters within the inner coma, separated by relatively long periods with no detected impacts as was seen during the encounter with comet Wild 2 in 2004. The nature of these clusters is, however, slightly different. At Wild 2 the impacts occurred in discrete 'swarms' with durations of a few seconds (corresponding to spatial scales of a few tens of km) with angular sizes of around 5°, comparable with those of narrow jets observed in the inner coma. These swarms were themselves composed of 'bursts' of events of duration around 0.1 s (less than a km in spatial extent) interpreted as expanding clouds of fragments from larger particles. If the grain fragmentation occurred far from the nucleus, outside the region where gas drag is significant, both small (micron-sized for PVDF) and large (>50 μm for acoustic) fragments were seen ('correlated' swarms). If the fragmentation occurred close to the nucleus, then size-dependent acceleration from the gas drag will separate the small and large fragments, resulting in 'uncorrelated swarms' where the spacecraft trajectory only passes through a narrow size range of fragments (Tuzzolino et al., 2004; Green et al., 2004; Clark et al., 2004). The spatial resolution at Tempel 1 is somewhat lower than at Wild 2 (0.1 s corresponds to 1.09 km rather than 612 m) but is still sufficient to separate bursts and swarms if present on the same scales as Wild 2. While the

Tempel 1 data show the same evidence for widespread grain fragmentation, clustering in jets ('swarms') is less apparent that at Wild 2. The 1 s resolution data close to the nucleus do not show discrete swarms (a jet with angular size of 5° would have duration of about 2 s). There is however, evidence for correlated (e.g. at -1 s) and uncorrelated (e.g. at +3 s) peaks in the impact rates between the small and large particles. The bursts of events in 0.1 s resolution data (Fig. 7c) have durations of several 10ths of a second (spatial scales of a few km), rather larger than those seen at Wild 2 which appeared to be unresolved despite the lower encounter speed.

The lack of detection of small or large particles does not imply their complete absence in any particular region of the coma. We have different sensitivity and different effective areas for small (detected with PVDF sensors) and large particles (detected with acoustic sensors). If the mass distribution index, α, is low, then the mass distribution is flat and we can detect large particles with the acoustic sensor entirely consistent with no detections from the PVDF sensors. If the mass index is high then we would expect to see small particles more easily. A more extensive demonstration is provided by Green et al. (2004). The observation that we have no small particles after 250 km implies that the mass index is low in this region.

The Tempel 1 results support the conjecture (Green et al., 2004) that swarms and bursts may be present in all cometary comae (hitherto unseen because of the lack of spatial resolution). However, it is also clear that there are still differences in the coma morphology between comets, perhaps as a result of differing levels of activity, surface morphology, and possibly composition. Comet 103P/Hartley 2 provided direct evidence for large icy particles in the inner coma (A'Hearn et al., 2011) which may form the parent bodies for fragmentation in this comet, but similar particles were not seen with the same camera system during Deep Impact flyby of Comet Tempel 1, probably due to insufficient camera resolution at the flyby distance. The differences

497 between the Tempel 1 and Wild 2 DFMI data may be because the activity levels at the time of
498 the Tempel 1 encounter were lower (the jets are much less pronounced in the Tempel1 images
499 (Farnham et al., 2012) than at Wild 2 (Sekanina et al., 2004), or because the spacecraft trajectory
500 did not pass through the jets. The DFMI certainly did not detect any jet activity. Similarly,
501 Farnham et al., (2012), by studying the camera images from the closest approach they have
502 found multiple jets, some of them very diffused and others very much collimated, but came to
503 the same conclusion that the Stardust-NExT did not pass thought any dust jets during the entire
504 encounter.
505
506 **4.3 Void analysis**
507
508 We can define "primaries" as the particles emitted directly from the nucleus. In the
509 classical model of dust coma production, all objects in the coma have been viewed as primaries,
510 whether sub-micron or meter-sized. These may be emitted omni-directionally or in preferred
511 directions, to form diffuse comae, fans and jets. Once a grain is accelerated a few radii from the
512 cometary nucleus by the concomitant conversion of ices to gas, it decouples and continues to
513 move outward more or less radially. In this classical view, the density of particles beyond the
514 innermost coma varies as $1/R^2$, where R is the distance from the nucleus.
515 In the new view, primaries, which are larger aggregates of particles are released and then
516 disintegrate further in the coma into secondary, tertiary, quaternary and higher-order particle
517 populations. The particle size distribution therefore evolves toward smaller particle dominance.
518 Jets and other structures may be, at least in part, manifestations of disintegration of aggregates in
519 the coma. However, because aggregates could also be emitted from a geometrically collimated

source, more information is needed to determine the relative importance of these distinct phenomena.

There is no simple way to distinguish successive generations of particles from parental aggregates. Although a smaller aggregate cannot be a progenitor of a larger aggregate, a large aggregate could fragment simply in a binary manner into many large fragments, as well as slowly erode to release smaller particles from itself or its progeny.

As seen in Fig. 8, the counts observed in successive time intervals and hence in discrete locations in the coma are mostly above or below that predicted by the classical $1/R^2$ model. Both positive and negative deviations are observed and can be instructive, with the excess counts being indicative of the proximity of larger aggregates and the shortfalls of counts being indicative of the dearth of small particle emission directly from the nucleus.

Within the data set, the occurrence of regions of the coma of Tempel 1 with no detectable particles over distances of 1 to 200 km along the Stardust NExT trajectory is striking. We define 'voids' as regions that register zero counts in any sensor. They may not necessarily be devoid of sub-micron particles below our detection threshold and if the sensors had had larger areas, other particle interaction events might have been registered. These regions are listed in Table 4. Forty of the 45 voids identified have expected counts from a uniform classical model in which the total fluence equals that detected by DFMI, of 7 to as high as 256. From the Poisson distributions for each of these, the probability of an observation with zero counts is 0.001 or less. Independent of the cases of excess counts, this alone is sufficient to falsify a hypothesis of pure classical emission for Tempel 1. Of further interest is whether some smaller portion of fine particulates could originate directly from the nuclear surface rather than as secondary emission from aggregates released into the coma. We have tested this in a number of ways, including selection

543 of void regions within cometocentric distances of 200 km to the closest approach to the nucleus
544 (178 km). For a probability of 0.01 that all six voids that occur within 200 km would each have
545 zero counts, the classical emission level must be ≤1.5% of the total emission of particles of size
546 m1 or larger. At larger distances before and after passing the nucleus (voids #2 and #33), a
547 confidence level of 99% for both of these zero count voids being observed is obtained for a limit
548 of 1.0% of total emission being classical. From both criteria, there is an even chance (probability
549 = 0.5) that the classical emission fraction is 0.25% or less of the total. These limits are
550 statistically-driven, and potentially could be shown to be lower by closer passages to a cometary
551 surface, flyby of a more active nucleus, and/or use of a particle detector with larger sensitive area
552 and shorter integration time (0.1 s).

553 In the passage through the coma of Tempel 1, a total of 38 "PVDF bursts", defined as
554 contiguous measurements of counts in ≥ m1 or M1, are detected by the PVDF sensors alone
555 (excluding acoustic sensor events). These are listed in Table 5. Of these, one-half have excess
556 counts over the classical model at ≥ 99% confidence level (all but two are ≥ 99.99%). For 14
557 additional events, the magnitude is significantly *less* than the expected number of counts but over
558 one-half of these have a time profile that indicates they also are discrete clusters. Five of the 38
559 events have counts that are not strongly distinguishable statistically from the counts predicted by
560 the classical model, and hence are not included in this analysis.

561 For the 19 excess count events, only rough estimates of starting mass can be made
562 because of lack of knowledge of which portion of a given cluster is being sampled during the
563 flythrough of the coma. However, using the same methodology as in Clark et al., (2004), the
564 masses of these obvious clusters range from 0.4 g to nearly 1 kg and are similar to results of the
565 Stardust flyby of Wild 2. These events are not thought to be due to jets because their collimation

would have to be less than 2° to 6°. Interestingly, relatively large acoustic events continue to occur post-closest approach, whereas no small particles are detected once the spacecraft is more than 250 km from the nucleus on the post-encounter side, with the exception of a single, isolated but distinct late particle event at 2940 km from the nucleus (see Event #38).

4.4 Dust mass distribution

From DFMI data we were able to derive the coma particle mass distribution for Comet Tempel 1, shown in Fig. 9 as a cumulative fluence for the whole encounter. There is good agreement, within the uncertainties, between the fluences derived from three independent sensor systems at masses 10^{-11} to 10^{-10} kg. The best fit mass distribution over the entire mass range yields a cumulative mass distribution index, $\alpha = 0.65$ (Fig. 9a). This would imply a coma where both the mass (when $\alpha<1$) and cross-sectional area (when $\alpha<0.67$) are dominated by the largest particles. However, there is evidence for a change in mass index at $m \sim 10^{-9}$ kg with a somewhat higher mass index at smaller masses and lower mass index above this mass (Fig. 9b). The break in the slope of the mass distribution coincides with the region sampled by the PVDF large sensor with the M2 detection and M3 and M4 upper limits somewhat lower than a smoothly varying mass index would imply and the M1 fluence somewhat lower than that defined by the PVDF small and acoustic sensor data at similar masses. Although there are uncertainties in the calibration due to likely differences in density and structure between the laboratory test particles and the cometary impactors, this might be expected to manifest itself in both the PVDF large and small sensor data. The small sensor data are in good agreement with the acoustic data where there is good signal to noise (i.e. more than a few impacts). A similar break in the mass distribution was seen

589 at comet Wild 2 (Green et al., 2004) with the same sensors, but in this case there was no
590 discrepancy between the small and large PVDF data. Also a similar change in mass distribution
591 was seen at comet Halley at similar particle masses but using different detectors and detection
592 techniques (McDonnell et al. 1991). While there may be a small systematic error in the
593 calibration transfer for the large PVDF sensors, this cannot account for the apparent slope change
594 measured by the acoustic sensors.

595 Fig. 9b shows a fit to the data with $m < 10^{-10}$ kg for which $\alpha = 0.87 \pm 0.08$. This is close
596 to the value seen for the same mass range during the entire P/Wild 2 encounter. However, at
597 Wild 2 the spacecraft detected a surge of impacts from small particles over 700 seconds post-
598 encounter. If these are excluded, then the mass distribution at Wild 2 for the equivalent
599 encounter period as at Tempel 1 was somewhat shallower, with $\alpha = 0.75$ Green et al., 2004). At
600 masses above ~10^{-9} kg, the mass index is not well defined, but is shallower than at low masses.
601 In common with Wild 2 and all other comets with in-situ dust detection, the total dust mass is
602 dominated by the larger particles in the coma. A comparison of the overall mass distribution
603 from the two comets visited by Stardust is shown in Fig. 10. As would be expected for a coma
604 characterized by clouds of fragmentation products, the mass distribution is highly variable along
605 the trajectory.

606

607 **5 Conclusions**

608

609 DFMI has provided dust flux measurements from the inner comae of two comets, both of which
610 exhibit highly non-uniform spatial distributions. The Stardust NExT encounter of comet Tempel
611 1 has revealed bursts of impacts of up to 1000 particles over km scales near closest approach

surrounded by void regions of many kilometers with no impacts. These data are consistent with passage through clouds of particles resulting from fragmentation of larger aggregates emitted from the nucleus. These fragmentation products dominate the total dust production of small particles, with only a small contribution likely from direct emission from the nucleus. The derived overall mass distribution is similar to that found at comet Wild 2 with the total mass dominated by large particles. The average cumulative mass index is 0.65 ± 0.08 but a better fit is obtained with an index of 0.85 ± 0.08 for particle masses below 10^{-10} kg and significantly lower for higher masses.

Acknowledgements

Work at the University of Chicago was supported by NASA subcontract with Cornell University NNM08AA26A. We thank Pasquale DiDonna for his help in analysis of the DFMI data at the University of Chicago. The acoustic sensor calibration and shield penetration experiments were performed by M.J. Burchell and B.A.M. Vaughan at the University of Kent.

References

A'Hearn, M.F., et al., 2011, EPOXI at Comet Hartley 2. Science 332, (6036), 1396-1400, http://dx.doi.org/10.1126/Science.1204054.

Brownlee, D. et al., 2006, Comet 81P/Wild 2 Under a Microscope. Science 314, (5806), 1711-1716.

Clark, B.C. et al., 2004, Release and Fragmentation of aggregates to produce heterogeneous, lumpy coma streams. *J. Geophys. Res.* 109, E12S03, http://dx.doi.org/10.1029/2004JE002319.

635 Economou, T.E, Green, S.F., Semenov, B.V., 2011. STARDUST 9P/TEMPEL 1 DFMI 2/3
636 NEXT V1.0, SDU-C/D-DFMI-2/3-NEXT-TEMPEL1-V1.0, NASA Planetary Data System.
637 Farnham, T.L., Bodewits, D., Li, J.-Y., Veverka, J., Thomas, P., Belton, M.J.S. 2012.
638 Connection between the jet activity and surface features on Comet 9P/Tempel 1.
639 http://dx.doi.org/10.1016/j.icarus.2012.06.019.
640 Green, S.F. et al., 2004. The dust mass distribution of Comet 81P/Wild 2. J. Geophys. Res. 109,
641 http://dx.doi.org/10.1029/2004JE002318.
642 Green, S.F. et al., 2007. Stardust wild 2 dust measurements. In: Krueger, H. and Graps, A.
643 (Eds.), Dust in Planetary Systems SP-643, ESA Publications, pp. 35-44.
644 Horz, F. et al., 2006. Impact craters and penetration tracks on Stardust: Implications for physical
645 properties, size-distribution and fluence of Wild 2 coma dust. Science, 314, 1716-1719.
646 McDonnell, J.A.M., et al., 2000. The stardust Dust Flux Monitor. Adv. Space Res. 25, 335-338.
647 McDonnell, J.A.M., Lamy, P.L., Pankiewicz, G.S., 1991. Physical properties of cometary dust.
648 In: Newburn, R.L., Neugebauer, M., Rahe, J.(Eds.), Comets in the Post-Halley Era. Kluwer,
649 Dordrecht, pp. 1043-1073.
650 McDonnell, T., McBride, N., Green, S.F., Ratcliff, P.R., Gardner, D.J., Griffiths, A.D., 2001. In:
651 Grun, E., Gustafson, B.A.S., Dermott, S.F. & Fechtig, H., (Eds.), Near Earth Environment.
652 In Interplanetary Dust. Springer, pp. 163-231.
653 Perry, Christopher H., In situ dust mass distribution measurements from the Giotto encounter
654 with comet P/Halley. Ph.D. Thesis Kent University, Canterbury (England), 1990.
655 Price, M.C. et al., 2010. Comet 81P/Wild 2: The size distribution of finer (sub 10-micrometer)
656 dust collected by the Stardust spacecraft. Meteorit. & Planet. Sci., 45, 1409-1428.

Tuzzolino, A.J. et al., 2003. Dust Flux Monitor Instrument for the Stardust mission to comet Wild 2. J. Geophys. Res. 108, http://dx.doi.org/10.1029/2003JE002086.

Tuzzolino, A.J. et al., 2004. Dust measurements in the coma of comet 81P/Wild 2 by the Dust Flux Monitor Instrument. Science 304, 1776-1780.

Sekanina, Z., Brownlee, D.E., Economou, T.E., Tuzzolino, A.J., Green, S.F., 2004. Modelling the nucleus and jets of comet 81P/Wild 2 based on the Stardust encounter data. Science 304, 1769-1774.

Simpson, J. A., Tuzzolino, A.J., 1985. Polarized polymer films as electronic pulse detectors of cosmic dust particles, Nucl. Instrum. Methods Phys. Res. Sect. A 236, 187– 202.

Walker, J.D., Chocron, S., 2011. Momentum enhancement in hypervelocity impact. Int. J. Impact Eng. 38, A1-A7.

Tables

Table 1. Comparison of effective areas for the DFMI channels at the 81P/Wild 2 and 9P/Tempel 1 encounters and 9P/Tempel 1 mass fluences for all 12 DFMI counters.

Sensor/ Channel	[a]Wild 2 Threshold (kg)	Tempel 1 Threshold (kg)	Effective area (m^2)	[b]Number of impacts	[c]Cumulative Fluence (counts/$m^{2)}$
PVDF Small					
m1	9.8×10^{-15}	2.6×10^{-15}	0.002	4173	$(2.45 \pm 0.04) \times 10^{6}$
m2	1.2×10^{-13}	3.2×10^{-14}	0.002	451	$(3.60 \pm 0.13) \times 10^{5}$
m3	4.3×10^{-12}	3.6×10^{-13}	0.002	266	$(1.34 \pm 0.08) \times 10^{5}$
m4	6.3×10^{-10}	5.3×10^{-11}	0.002	2	$(1.0 \pm 0.7) \times 10^{3}$
PVDF Large					
M1	8.5×10^{-11}	1.2×10^{-11}	0.02	13	$(7.0 \pm 1.9) \times 10^{2}$
M2	1.7×10^{-9}	2.5×10^{-10}	0.02	1	$(5 \pm 5) \times 10^{1}$
M3	1.4×10^{-8}	2.0×10^{-9}	0.02	0	$<5.5 \times 10^{1}$
M4	1.5×10^{-7}	2.2×10^{-8}	0.02	0	$<5.5 \times 10^{1}$
Acoustic Front					
AC_1	3×10^{-11}	$(1.3\ ^{+3}/_{-1}) \times 10^{-11}$	[d]variable	[e]125	[f] $(8.7\ ^{+2.4}/_{-1.3}) \times 10^{2}$
AC_2	3×10^{-10}	$(1.3\ ^{+3}/_{-1}) \times 10^{-10}$	[d]variable	[e]61	[f] $(4.2 \pm 0.5) \times 10^{2}$
Acoustic Rear					
AC_3	2×10^{-7}	$(6\ ^{+6}/_{-4}) \times 10^{-8}$	$0.3\ ^{+0.4}/_{-0.2}$	[e]17	$(5.7\ ^{+11.4}/_{-3.5}) \times 10^{1}$
AC_4	2×10^{-6}	$(6\ ^{+6}/_{-4}) \times 10^{-7}$	$0.3\ ^{+0.4}/_{-0.2}$	[e]4	$(1.3\ ^{+2.8}/_{-1.0}) \times 10^{1}$

[a] From Tuzzolino *et al.* (2004) Table 1 with factor 10^3 error in AC_3, AC_4 corrected.
[b] PVDF and Acoustic impact numbers are cumulative in mass for each sensor.
[c] Number of impacts per m^2 for $m >$ threshold mass.
[d] Effective area depends on the mass distribution (see text)
[e] Number of impacts not directly measured (see Sections 2.2 and 4.1 for details)
[f] Calculated using effective area = 0.144 m^2 corresponding to α=0.65

Table 2. Comparison of Internal Flight Pulser Calibrations (IFC) counts in DFMI counters for different periods during Stardust and Stardust NExT missions.

11/2/2002	IFC							
	M1	M2	M3	M4	m1	m2	m3	m4
	0	0	0	0	0	0	0	0
	267	1	0	0	238	1	1	0
	499	221	1	0	378	138	1	0
	806	486	257	1	834	474	292	1
FINAL	963	647	418	162	1021	635	453	162
8/12/2010	IFC							
	M1	M2	M3	M4	m1	m2	m3	m4
	0	0	0	0	0	0	0	0
	266	1	0	0	235	1	1	0
	499	222	1	0	378	144	1	0
	804	486	256	1	835	473	278	1
FINAL	965	647	417	162	1006	634	439	162
2/2/2011	IFC							
	M1	M2	M3	M4	m1	m2	m3	m4
	0	0	0	0	0	0	0	0
	266	1	0	0	232	1	1	0
	499	222	1	0	374	143	1	0
	804	486	256	1	832	473	281	1
FINAL	964	647	417	162	1008	634	442	162

Table 3. Samples of Acoustic sensor data. See text for explanation of interpretation to define number of impacts.

Record #	Time[a] (sec)	Δt[b] (sec)	Acoustic sensor counts				Assigned impacts			
			AC_1	AC_2	AC_3	AC_4	N_1	N_2	N_3	N_4
919										
920	-396.6	1.000	2				1			
921										
. . .										
1238										
1239	-77.684	0.898	47	12			1	1		
1240	-77.582	0.102	22				1			
1241										
. . .										
1268										
1269	-51.797	0.600	20	38			2	1		
1270	-51.594	0.203	60	18						
1271										
. . .										
1281										
1282	-39.594	1.000	4				1			
1283	-39.297	0.297	119	142	80	41	2	2	1	1
1284	-38.582	0.700	1		18					
1285	-38.281	0.301	23	9	5		1	1	1	
1286	-37.582	0.699	41				1			
1287	-36.578	1.004	2				1			
1288										

[a]Time from encounter (4h 39m 12s)
[b]Duration of record

750 **Table 4**. Void regions, wherein no particles were detected by any sensor.

Void Number	Time to Encounter (s)	Delta Time (s)	Start Distance (km)	End Distance (km)	Relative Longitude on Comet (deg)	Expected Counts (1/R^2)	Poisson Probability (0 counts)
1	-398.0	116.0	4342.3	3079.4	-65.9	22.7	1.38E-10
2	-263.0	185.9	2872.6	859.3	-55.9	195.8	9.00E-86
3	-76.4	6.4	851.8	783.9	-23.2	24.6	2.09E-11
4	-69.0	12.0	773.3	646.7	-21.2	61.4	2.20E-27
5	-56.0	1.0	636.2	625.6	-17.5	6.5	1.54E-03
6	-54.4	0.4	619.4	615.2	-17.0	2.7	6.67E-02
7	-53.0	1.0	604.8	594.4	-16.6	7.0	8.91E-04
8	-51.0	1.0	584.1	573.6	-16.0	7.8	4.18E-04
9	-49.0	1.0	563.2	552.9	-15.4	8.2	2.88E-04
10	-47.0	4.0	542.6	501.6	-14.8	37.2	6.79E-17
11	-42.0	2.0	491.4	471.3	-13.3	21.7	3.81E-10
12	-36.0	1.0	431.1	421.2	-11.4	13.8	1.02E-06
13	-34.0	1.0	411.5	401.7	-10.8	15.2	2.52E-07
14	-32.0	1.0	391.8	382.2	-10.2	16.7	5.40E-08
15	-30.0	2.0	372.6	353.7	-9.6	38.1	2.91E-17
16	-27.0	1.0	344.3	334.9	-8.6	22.1	2.49E-10
17	-23.0	1.0	307.7	299.0	-7.4	27.4	1.25E-12
18	-21.0	2.0	290.3	273.3	-6.7	63.6	2.29E-28
19	-18.5	1.5	269.2	257.1	-5.9	54.8	1.59E-24
20	-14.3	0.3	236.9	234.6	-4.6	14.6	4.67E-07
21	-12.6	0.6	225.0	221.1	-4.1	30.7	4.54E-14
22	-8.0	1.0	198.3	193.8	-2.6	65.4	3.80E-29
23	-6.7	0.7	192.5	189.7	-2.2	49.4	3.66E-22
24	-4.0	1.0	183.4	181.1	-1.3	77.1	3.21E-34
25	0.4	0.7	178.0	178.4	0.1	58.1	6.02E-26
26	1.7	0.3	178.9	179.3	0.5	23.5	6.45E-11
27	3.9	0.1	182.9	183.2	1.2	8.0	3.34E-04
28	12.9	0.1	226.7	227.4	4.1	5.3	4.92E-03
29	13.9	0.1	233.5	234.2	4.5	5.0	6.57E-03
30	15.5	1.5	245.1	256.8	5.0	66.3	1.66E-29
31	23.0	2.0	307.3	325.3	7.4	55.8	5.63E-25
32	26.0	1.0	334.3	343.6	8.3	24.2	3.02E-11
33	28.0	17.0	353.1	521.4	8.9	256.1	5.98E-112
34	46.0	4.0	531.8	572.9	14.5	35.7	3.03E-16
35	51.0	2.0	583.3	604.3	16.0	15.6	1.62E-07
36	54.0	3.0	614.7	645.9	16.9	20.4	1.33E-09
37	58.0	1.0	656.6	667.0	18.0	6.2	2.01E-03
38	60.0	10.0	677.6	783.3	18.6	51.1	6.39E-23
39	71.0	3.0	793.9	825.6	21.7	12.3	4.58E-06
40	75.0	5.0	836.2	889.5	22.8	18.1	1.31E-08
41	81.0	15.0	900.2	1061.0	24.5	42.3	4.32E-19
42	97.0	3.0	1071.7	1104.0	28.6	6.8	1.10E-03
43	101.0	39.0	1114.8	1535.9	29.6	61.0	3.17E-27
44	141.0	27.0	1546.7	1839.4	38.4	25.3	1.01E-11
45	169.0	86.0	1850.2	2784.7	43.5	44.4	5.26E-20

751

Table 5. PDVF Events are categorized by whether there is an Excess of counts above the expected value from the classical model, Nominal (near expected value), or Low in counts. The Standard Deviations column is the ratio of the observed difference between expected and actual counts, divided by the standard deviation (square root) of the expected counts.

PVDF Event #	Type of Event	Time to Encounter (s)	Event Duration (s)	Start Distance (km)	Event Distance (km)	Relative Longitude on Comet (deg)	Expected m1 Counts (1/R^2)	Actual m1 Counts	Number of Standard Deviations	M1 Counts	Mass g
1	**Excess**	-78.0	0.9	868.9	9.8	-23.7	**3.1**	**62**	33.5		51.5
2	Nominal	-77.0	0.6	858.2	6.6	-23.4	2.1	1	-0.8		0.4
3	**Excess**	-70.0	0.3	783.9	3.2	-21.5	**1.3**	**27**	23.0		2.4
4	Nominal	-55.0	0.6	625.6	6.6	-17.2	4.0	1	-1.5	3	
5	Nominal	-52.0	0.8	594.4	8.6	-16.3	5.8	4	-0.8		
6	**Excess**	-39.0	0.3	461.2	3.2	-12.4	**3.6**	**121**	61.9		11.0
7	**Excess**	-38.0	0.3	451.1	3.3	-12.1	**3.8**	**42**	19.5		3.9
8	**Excess**	-30.4	0.7	382.2	7.7	-9.7	**12.4**	**95**	23.4		48.3
9	Nominal	-28.0	0.4	353.7	4.3	-9.0	8.2	10	0.6		
10	Low	-24.0	1.9	325.7	20.7	-7.7	47.2	21	-3.8		
11	**Excess**	-22.0	0.8	299.0	8.7	-7.1	**22.8**	**126**	21.6		82.3
12	Low	-19.0	0.5	273.3	5.5	-6.1	17.1	1	-3.9		
13	**Excess**	-17.0	0.6	257.1	6.6	-5.5	**23.2**	**70**	9.7		26.1
14	Low	-14.5	0.7	242.0	7.6	-4.7	30.9	1	-5.4		
15	**Excess**	-13.0	1.4	234.6	15.3	-4.2	**67.2**	**123**	6.8		248.8
16	**Excess**	-12.0	0.8	221.1	8.7	-3.9	**42.4**	**59**	2.5		38.9
17	**Excess**	-10.8	0.7	214.8	7.7	-3.5	**40.2**	**313**	43.0		159.2
18	**Excess**	-9.8	0.3	208.9	3.2	-3.2	**17.9**	**260**	57.2		23.6
19	**Excess**	-9.0	0.1	203.4	1.1	-2.9	**6.1**	**19**	5.2		0.2
20	Low	-7.0	0.3	193.8	3.3	-2.3	20.6	1	-4.3		
21	Nominal	-6.0	0.9	189.7	9.8	-1.9	65.1	70	0.6		
22	Low	-3.0	0.6	181.1	6.5	-1.0	47.4	10	-5.4		
23	**Excess**	-0.6	1.6	179.4	17.4	-0.2	**131.2**	**172**	3.6		451.6
24	**Excess**	0.3	0.4	178.0	4.3	0.1	**33.1**	**1025**	172.4		167.4
25	Low	1.6	0.7	178.3	7.6	0.5	57.9	12	-6.0		
26	Low	2.7	0.9	179.3	9.8	0.9	73.4	38	-4.1		
27	**Excess**	3.8	0.9	180.9	10.0	1.2	**73.1**	**1126**	123.1		967.8
28	**Excess**	4.5	0.7	183.2	7.6	1.4	**54.8**	**123**	9.2		61.9
29	Low	5.3	0.6	186.1	6.5	1.7	45.4	28	-2.6		10.3
30	Low	6.2	0.4	189.6	4.3	2.0	29.2	15	-2.6		
31	**Excess**	7.5	0.6	193.6	6.5	2.4	**42.2**	**96**	8.3		35.3
32	Low	8.3	0.5	198.0	5.5	2.7	33.9	10	-4.1		
33	**Excess**	9.0	0.1	203.0	1.1	2.9	**6.3**	**55**	19.4		0.5
34	Low	12.2	1.9	214.5	20.7	3.9	105.6	21	-8.2		
35	Low	13.1	0.9	227.4	9.6	4.2	44.9	2	-6.4	1	
36	Low	14.0	0.2	234.2	2.2	4.5	9.6	0	-3.1	1	
37	Low	15.0	0.5	241.4	5.4	4.8	23.0	0	-4.8	2	
38	**Excess**	269.0	0.5	2937.0	5.5	56.5	**0.2**	**13**	32.8		3.3

Figure Captions:

Fig. 1. a) Schematic of the Stardust spacecraft showing the location of the PVDF and Acoustic Dust Sensors**. b)** Location of acoustic sensor A2 on the Acoustic (NEXTEL) plate. **c)** Location of the DFMI sensor unit (SU) and acoustic sensor A1 on the front Bumper panel. The A1 sensor is mounted to the underside of the Bumper plate.

Fig. 2. Schematic of DFMI acoustic sensor output voltage V as a function of time. Vp is the peak voltage. The acoustic sensor counts in channel 1 (or 2) are incremented by one for every time interval T_1 (T_2) in which the counts exceed the voltage threshold V_1 (V_2). The illustrated event, from one impact, would result in counts AC_1=3 and AC_2=3.

Fig. 3. Results for Stardust shield penetration experiments. The front shield exit hole area is plotted as a function of particle kinetic energy for normal impacts of different materials onto the front shield material. The cross indicates the estimated penetration energy.

Fig. 4. The effective area of the front shield acoustic sensors at the effective masses of channels AC_1 and AC_2, as a function of mass distribution index α.

Fig. 5. a) DFMI performance after an internal flight calibration in the first part of the spectrum (0-120 seconds). The instrument is then quiet for more than 2200 sec, when suddenly it becomes noisy due to an overheated power supply. The strategy throughout the rest of the mission was designed to overcome this behavior.

784 **b)** Comparison of the performance of the DFMI during the Stardust mission. The Internal Flight
785 Pulser Calibrations (IFC) of DFMI performed after Annefrank asteroid flyby in February 2003
786 and after the encounter with comet Wild 2 in January 2004 shows that the performance of the
787 DFMI has not changed.
788
789 **Fig. 6.** Three dimentional plot of count rates (z axis) for all DFMI counters as a function of time
790 (x axis) from the closest approach during the Tempel 1 encounter. The lightest dust particles
791 (m1 counter) are plotted in back, while the heaviest particles from AC4 counter are plotted in
792 front (y axis).
793
794 **Fig. 7.** Dust impacts detected by DFMI sensors through the Tempel 1 encounter on three
795 different time scales: a) PVDF m sensor and acoustic sensor impacts from -400 s to +300 s at 1 s
796 resolution, b) PVDF m sensor and acoustic sensor impacts from -100 s to +100 s at 1 s
797 resolution, c) PVDF m sensor data from -10 s to +10 s at 0.1 s resolution. Note the logarithmic
798 scales for the PVDF data in a) and b).
799
800 **Fig. 8.** Counts vs distance ($1/R^2$) distribution.
801
802 **Fig. 9.** The cumulative mass distribution of the dust particles registered by DFMI in the inner
803 coma during the encounter with comet 9P/Tempel 1. **a)** The best fit overall mass distribution
804 index of $\alpha = 0.65$ (where the fluence of particles with mass greater than m, $N(>m)=k\, m^{-\alpha}$) is
805 somewhat lower than that found for Wild 2. **b)** A better fit can be obtained with a two-slope
806 model with $\alpha = 0.87$ at lower masses (solid line) and a lower mass index (dashed line is $\alpha = 0.2$)

807 at higher masses. The uncertainties in the relative mass calibration, and the small number of
808 detected impacts, for penetrating particles mean the high mass slope is not well constrained.
809 .
810
811 **Fig. 10.** Comparison of DFMI data from Wild 2 (open symbols) and faint lines show fluence for
812 1200 seconds centred on closest approach) with the Tempel 1 encounter (solid symbols and bold
813 lines). Small squares are PVDF small sensor, large squares are PVDF large sensor and circles are
814 acoustic sensor data.
815
816

817 **Figure 1**

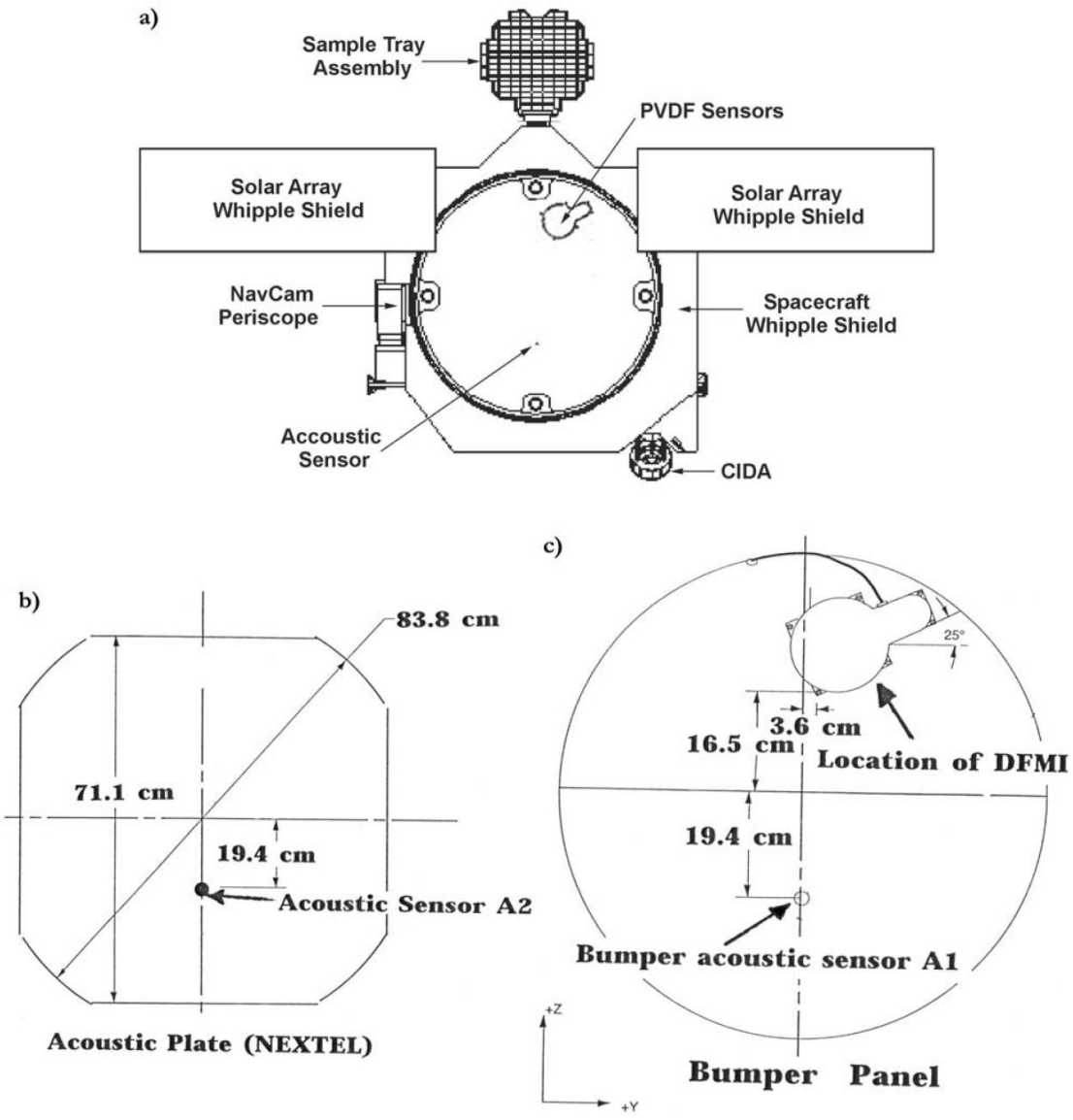

818

819

820 **Figure 2**

821

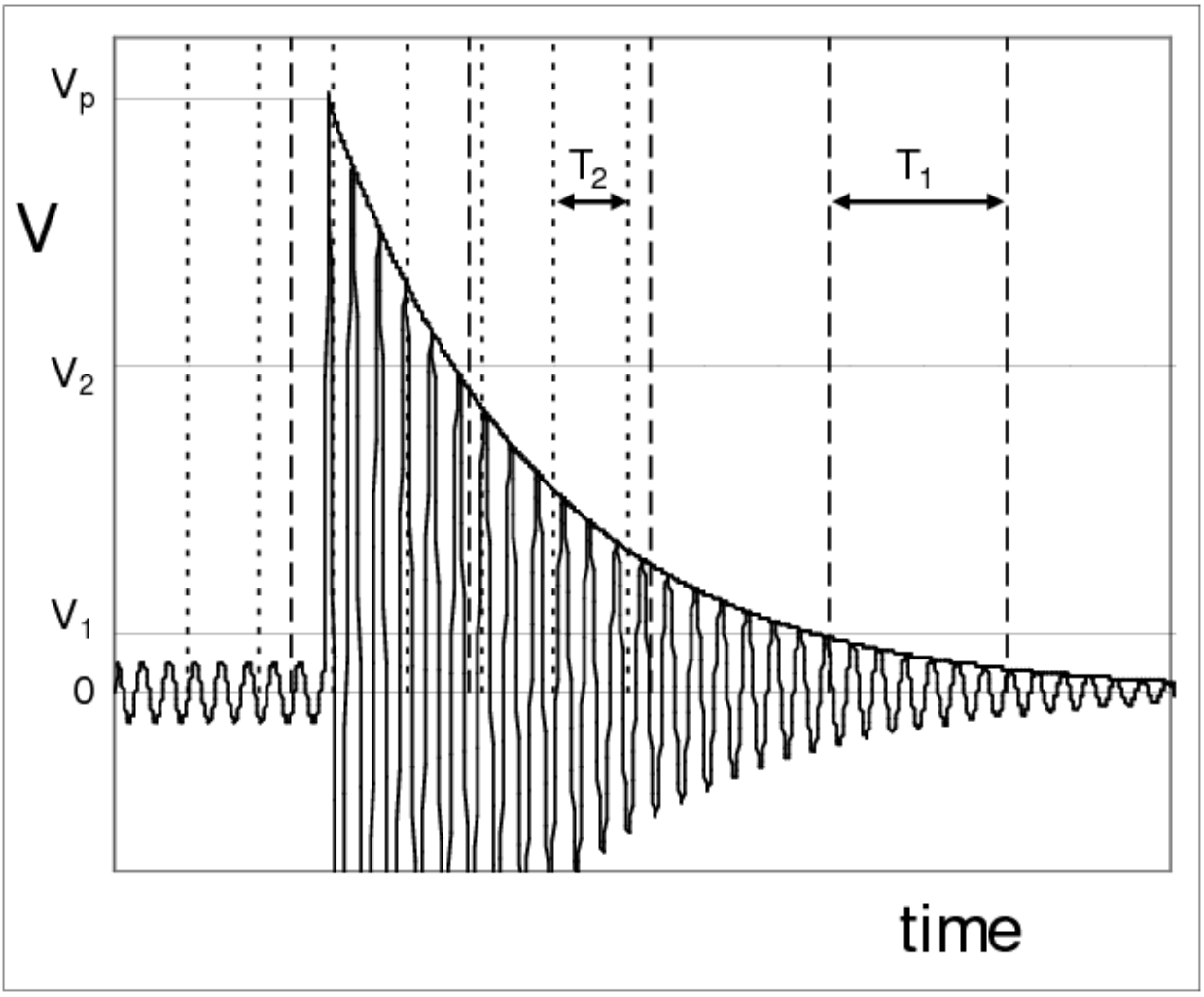

822

823

Figure 3

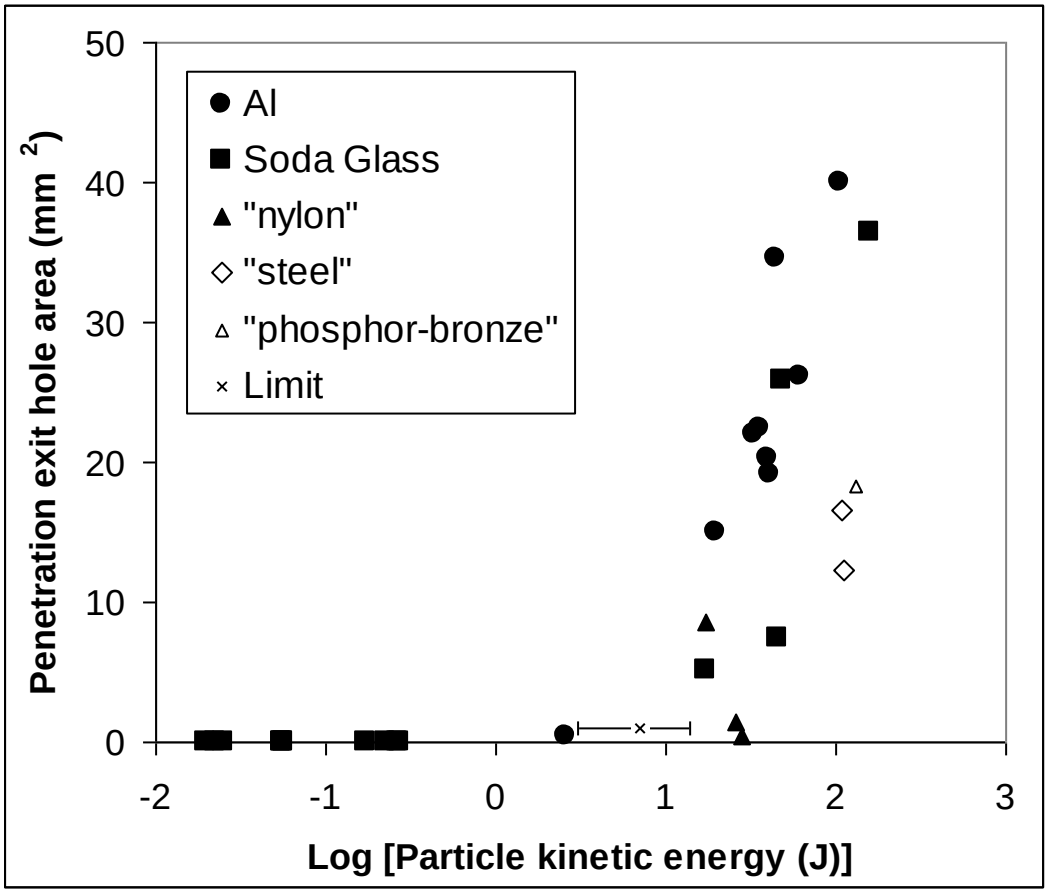
Al
Soda Glass
"nylon"
"steel"
"phosphor-bronze"
Limit
Penetration exit hole area (mm 2)
Log [Particle kinetic energy (J)]
50
40
30
20
10
0
-2
-1
0
1
2
3

836

837

838

839 **Figure 4**

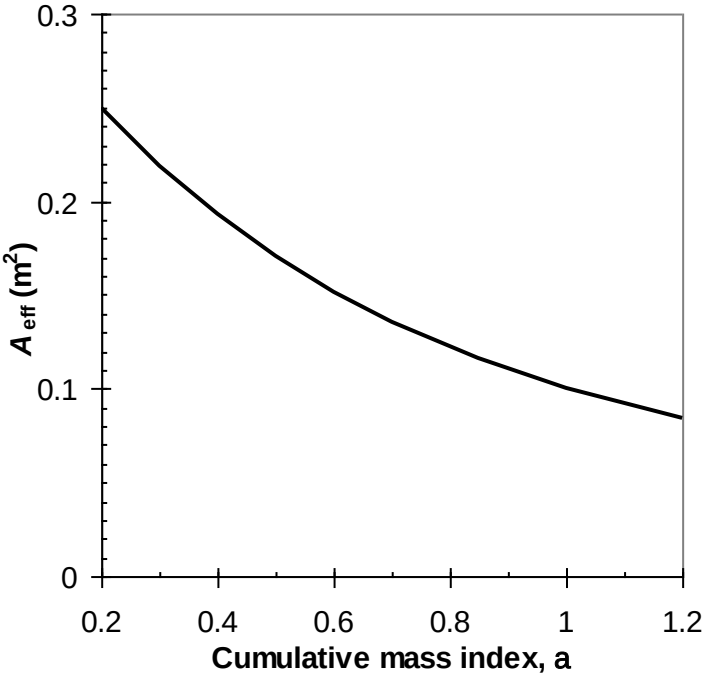

840

841

842 **Figure 5**

843 **a)**

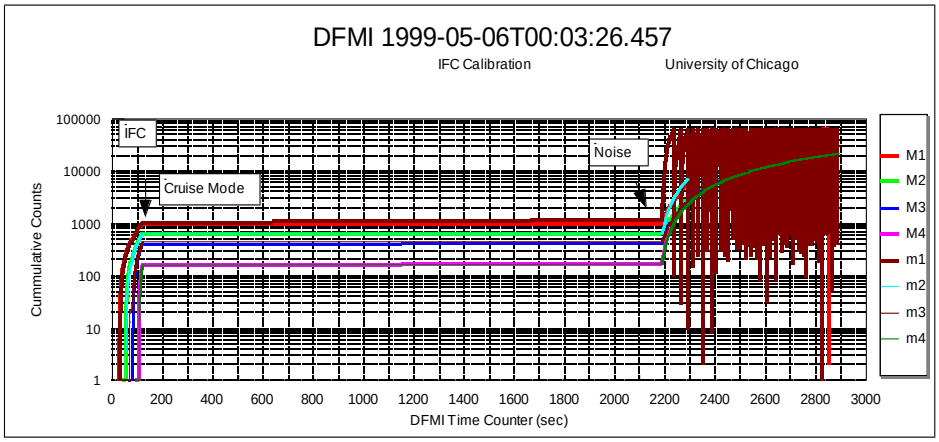

844

845 **b)**

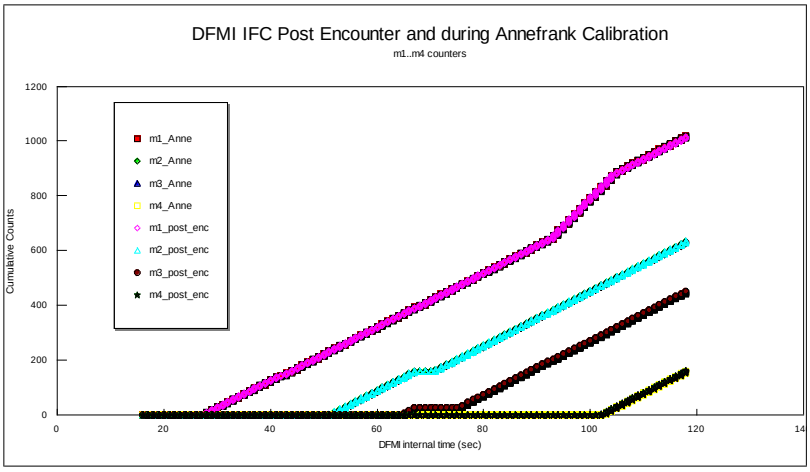

846

847 **Figure 6**

848

849

850

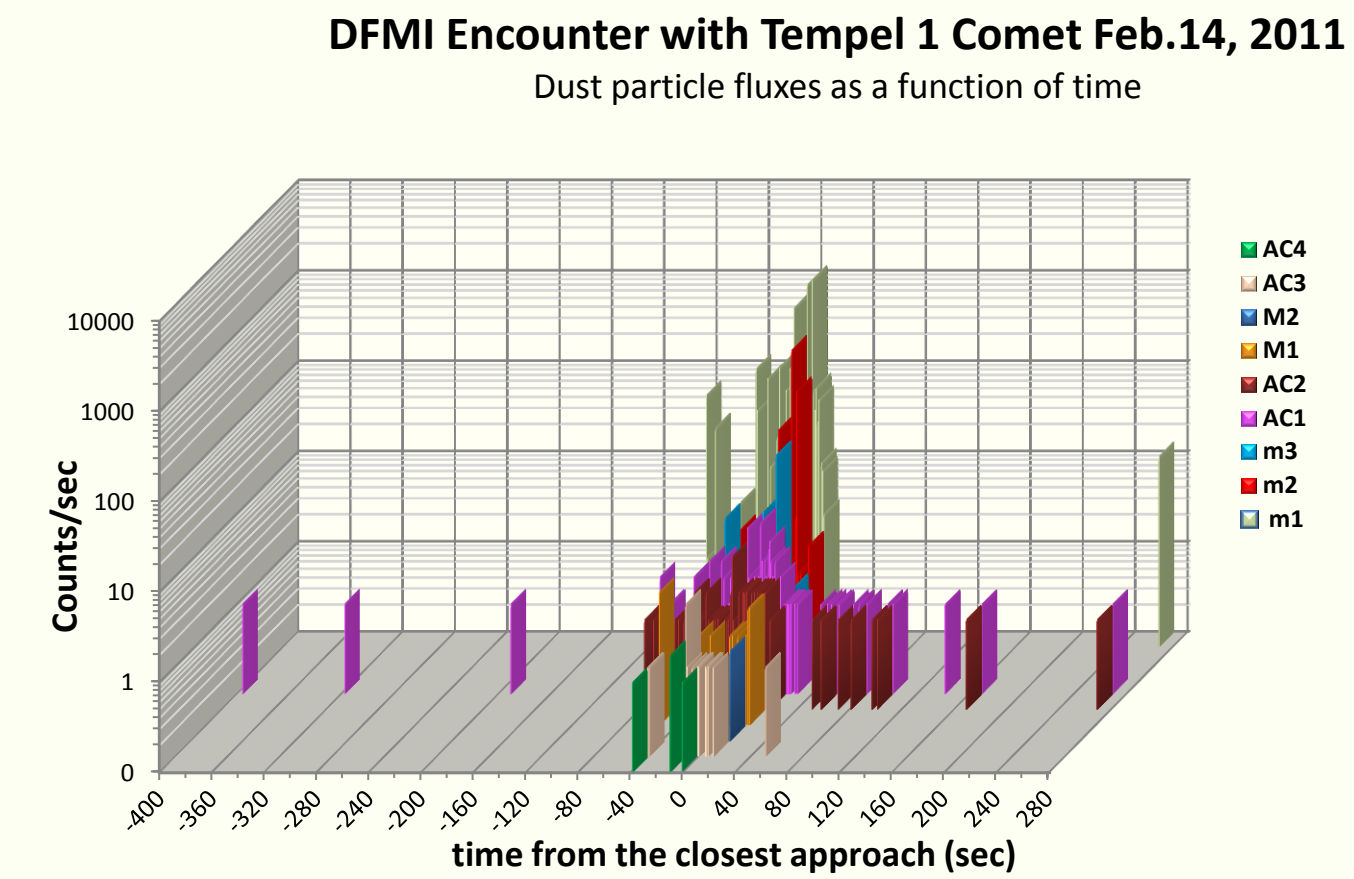

851

852

853

854

855 **Figure 7**

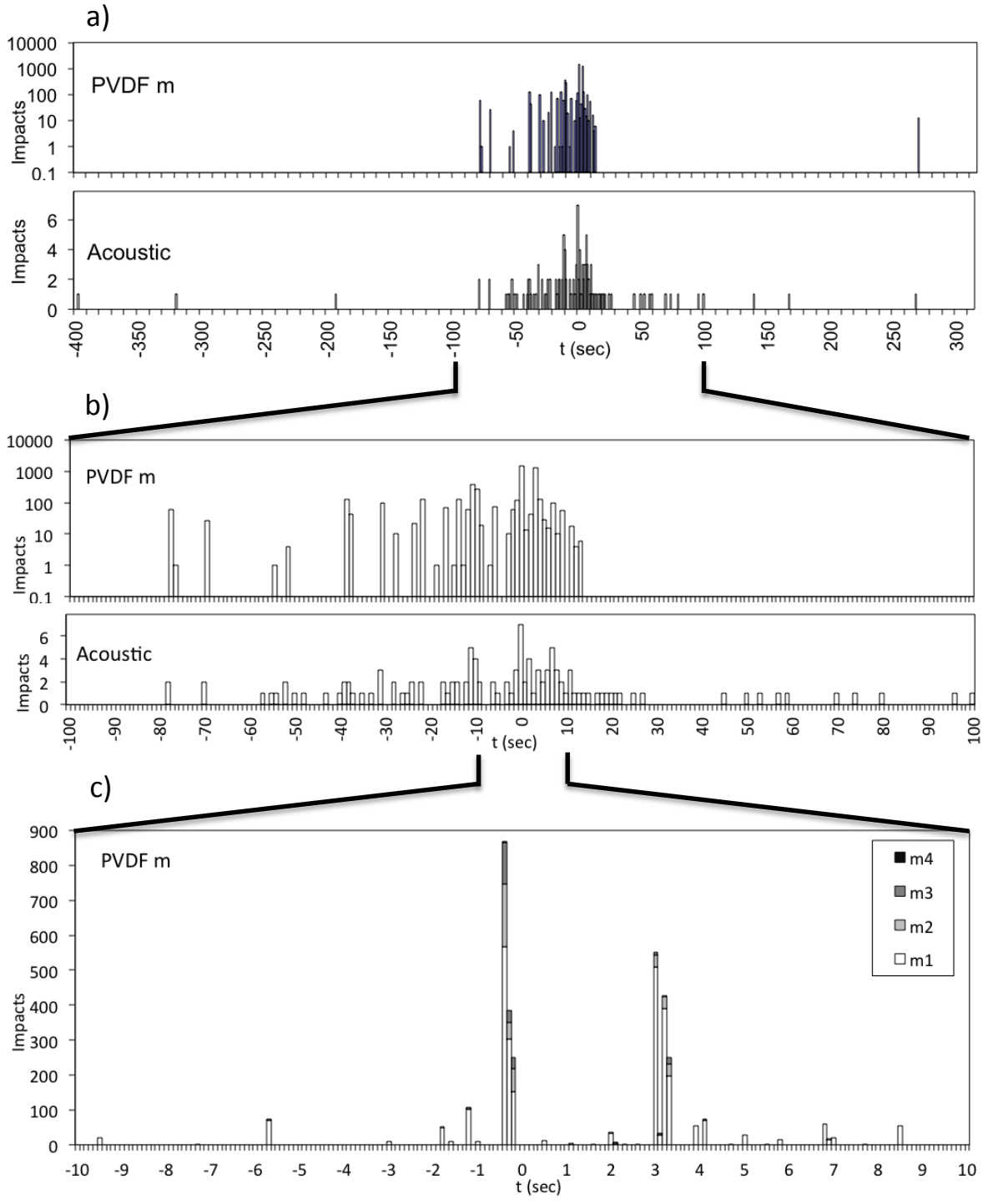

856

857

858

859 **Figure 8**

860

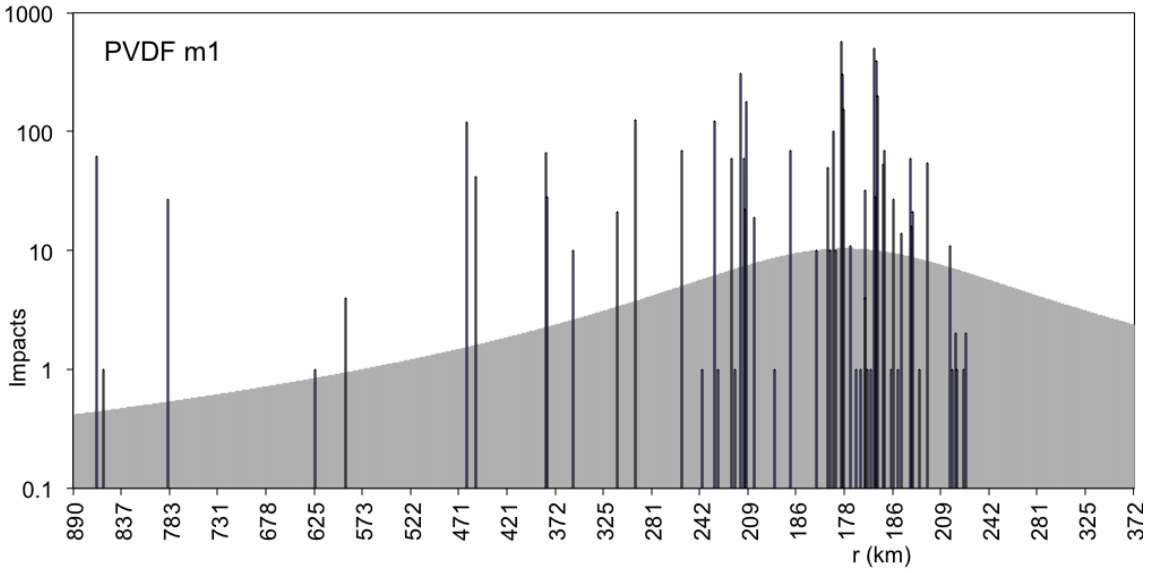

861

862

863

Figure 9

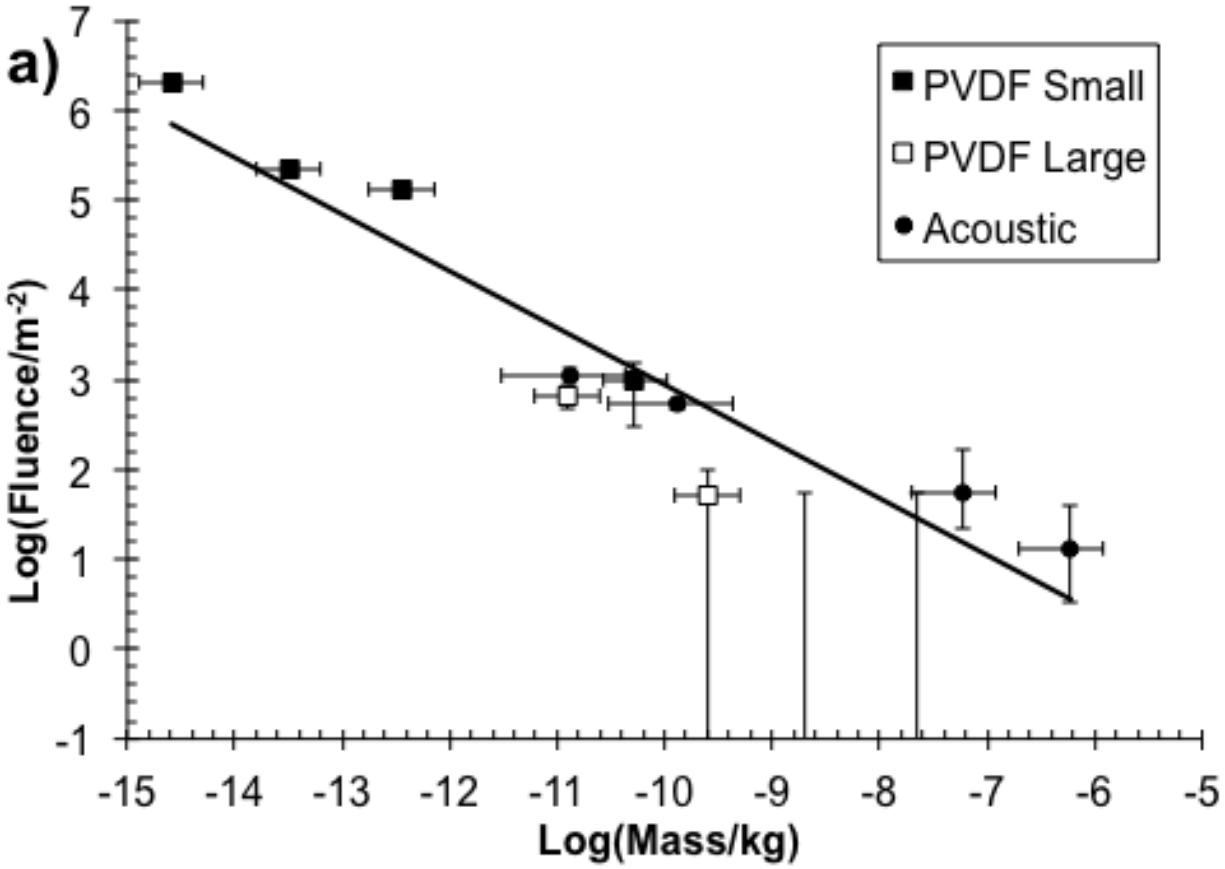
a)
PVDF Small
PVDF Large
Acoustic
Log(Fluence/m-2)
Log(Mass/kg)
7
6
5
4
3
2
1
0
-1
-15
-14
-13
-12
-11
-10
-9
-8
-7
-6
-5

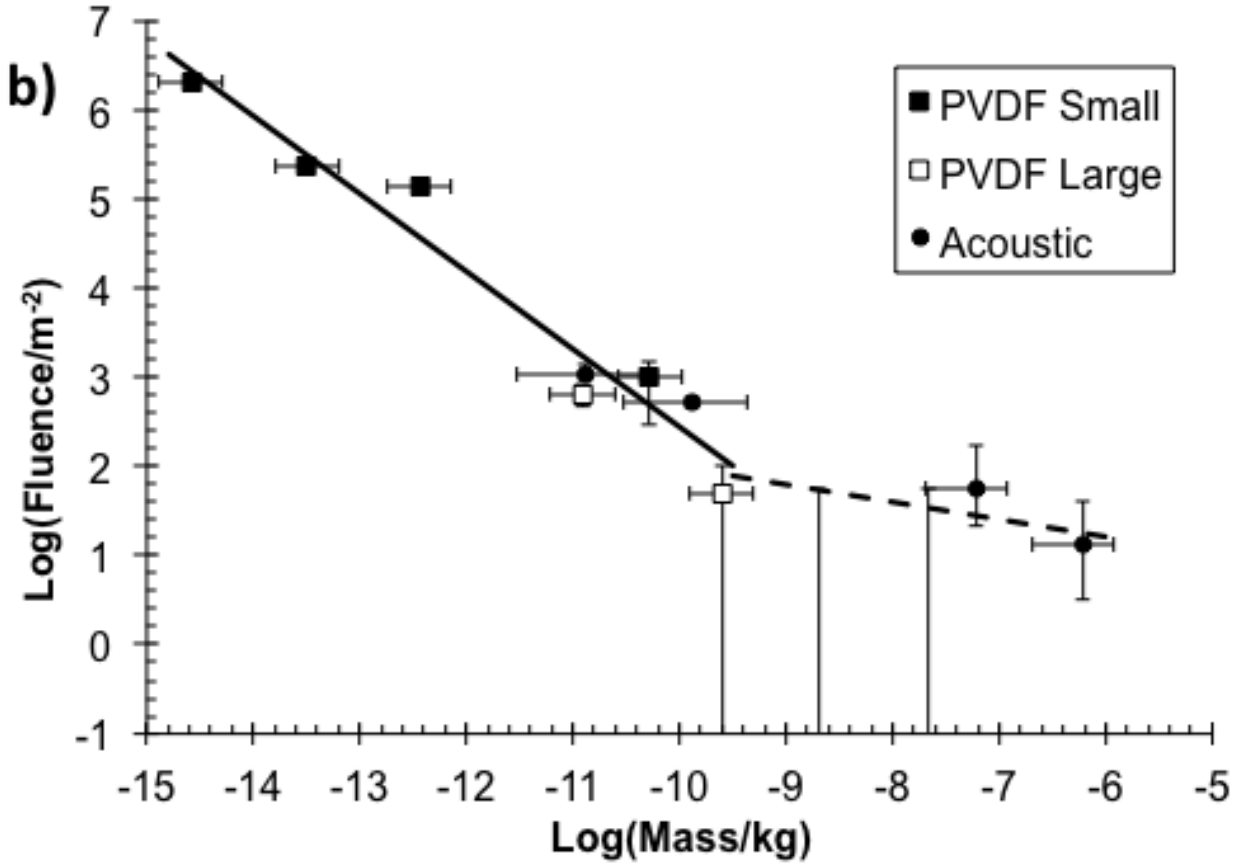
b)
PVDF Small
PVDF Large
Acoustic
Log(Fluence/m-2)
Log(Mass/kg)
7
6
5
4
3
2
1
0
-1
-15
-14
-13
-12
-11
-10
-9
-8
-7
-6
-5

883 **Figure 10**

884

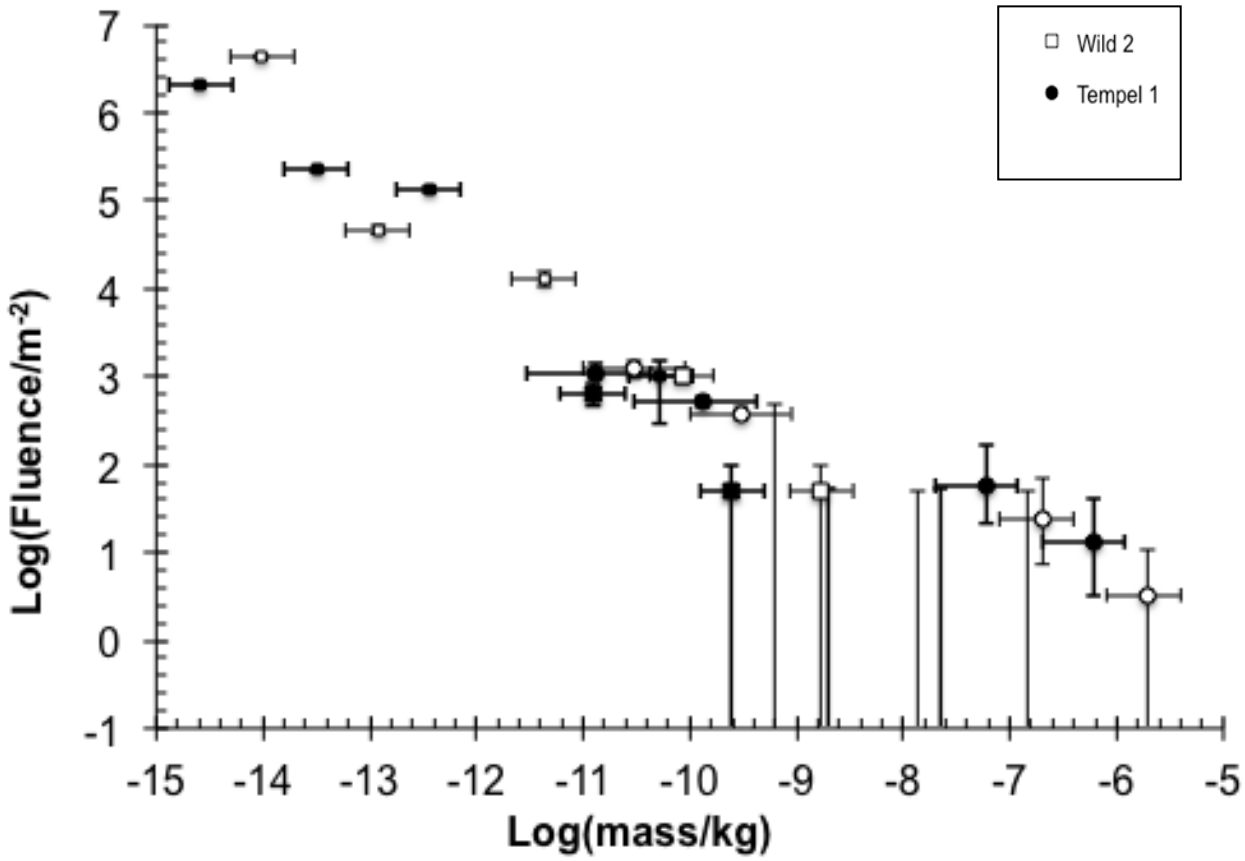

885
886
887